Supplementary Materials for

Multi-scale thermal homeostasis: Plants achieve temperature control through hierarchical regulation

The PDF file includes:

Supplementary Text
Figs. S1 to S12

Fig. S1.

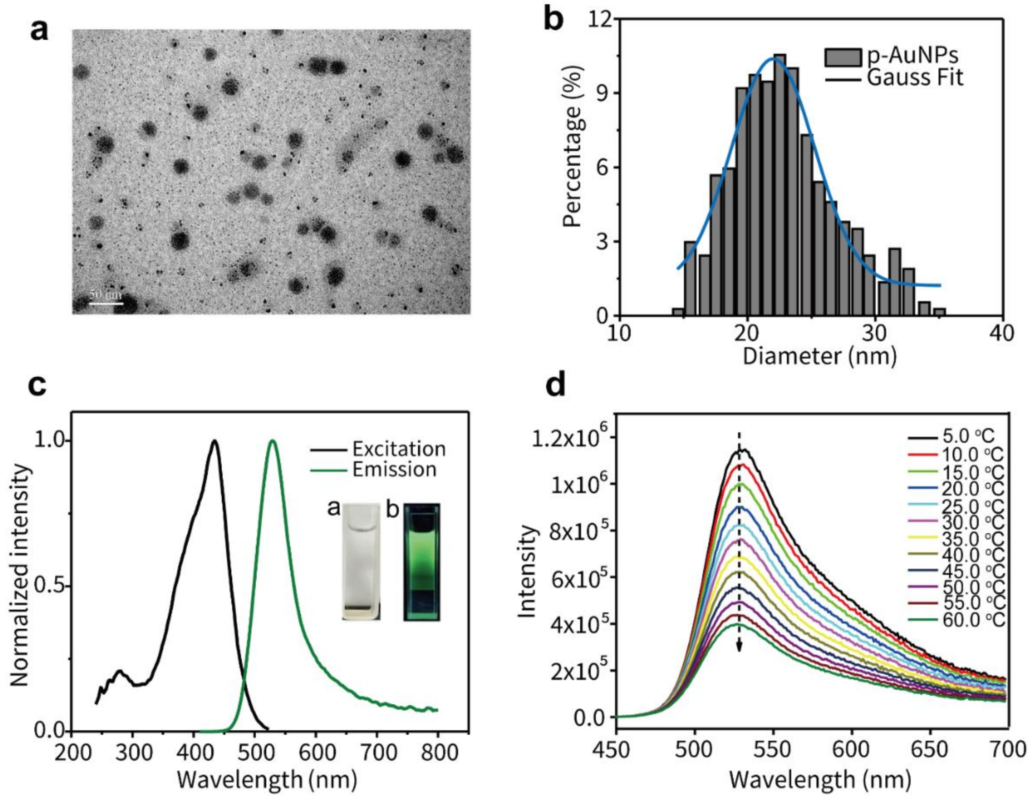

Fig. S1. Characterization of p-AuNPs.

a, Transmission electron microscopy (TEM) image of p-AuNP@HTT. **b**, The corresponding size distribution histogram (columns) and distribution curve (solid line) according to the result of TEM. **c**, The PL excitation (black curve, $\lambda_{emission}$ = 529 nm), and PL emission (green curve, $\lambda_{excitation}$ = 405 nm) spectra. Insert: The picture of p-AuNPs aqueous solution under natural and UV light. **d**, The temperature-dependent luminescent properties of p-AuNP@HTT. The PL emission ($\lambda_{excitation}$ = 405 nm) of p-AuNP@HTT obtained at different temperature ranging from 5 to 60°C.

Fig. S2.

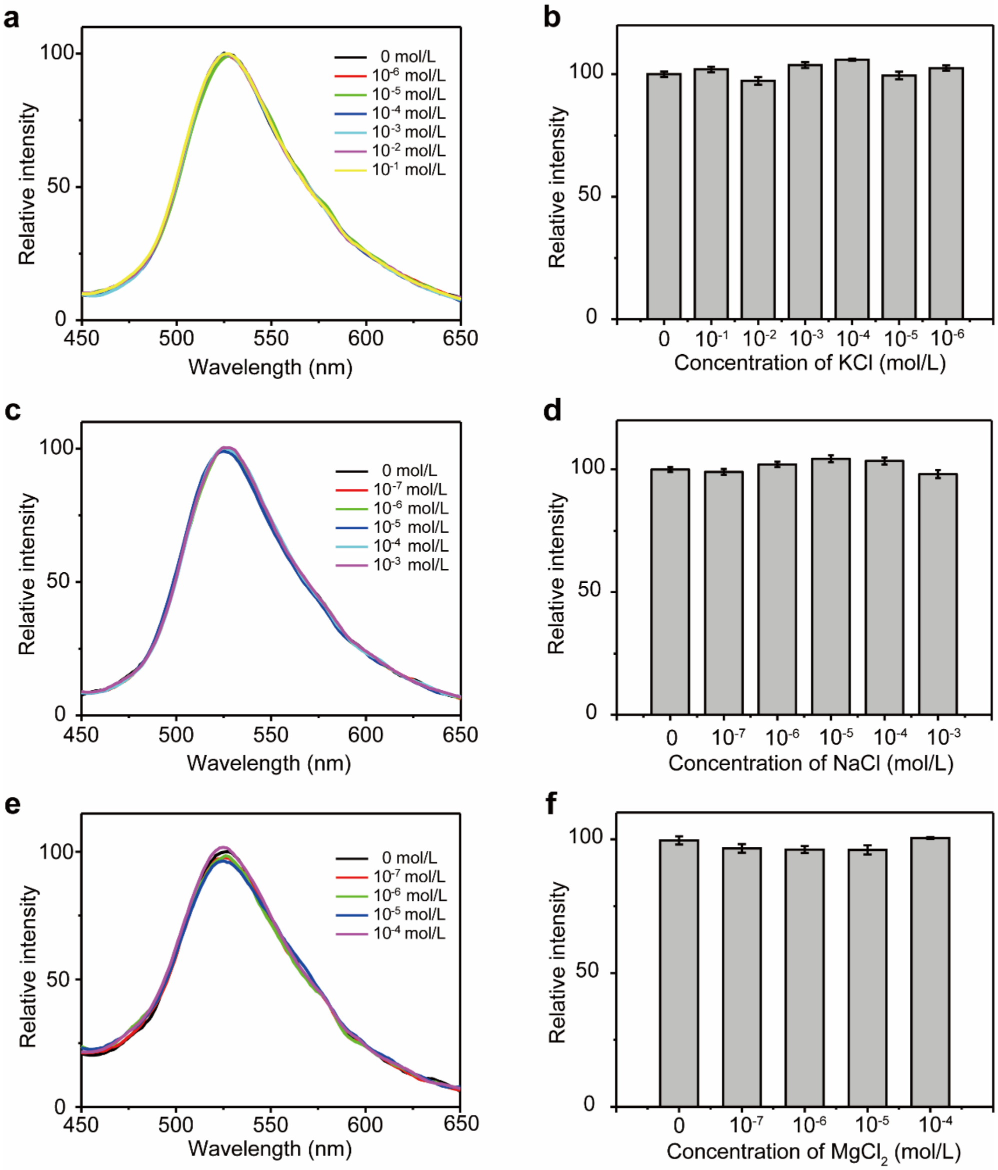

Fig. S2. The pH and ionic strength-dependent luminescent properties of p-AuNPs.

a, The PL spectra of p-AuNPs under different KCl concentrations, with no apparent spectral shift. **b**, The relative PL intensity of p-AuNPs as a function of KCl concentration. **c**, The PL spectra of p-AuNPs under different NaCl concentrations, with no apparent spectral shift. **d**, The relative PL intensity of p-AuNPs as a function of NaCl concentration. **e**, The PL spectra of p-AuNPs under different $MgCl_2$ concentrations, with no apparent spectral shift. **f**, The relative PL intensity of p-AuNPs as a function of $MgCl_2$ concentration. The error bars represent the standard deviations obtained from three parallel experiments.

Fig. S3.

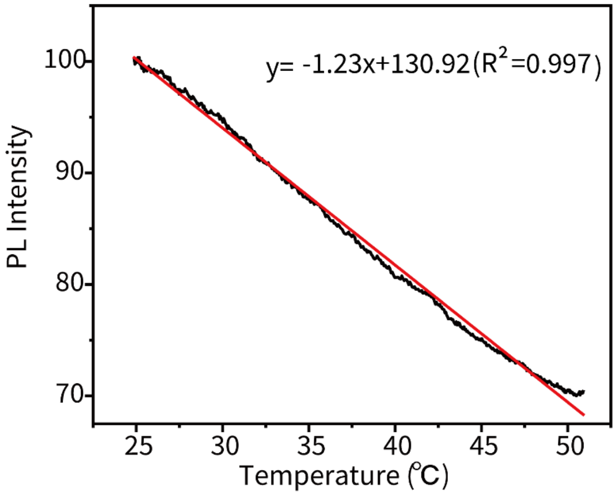

Fig. S3. The PL intensity of p-AuNPs as a function of temperature.
The dependence of photoluminescence (PL) from p-AuNP@HTT on time-gated imaging system (TGI), with a time delay of 100 ns. The fluorescence intensity changes linearly with temperature, decreasing by 1.23% for every 1°C increase in temperature.

Fig. S4.

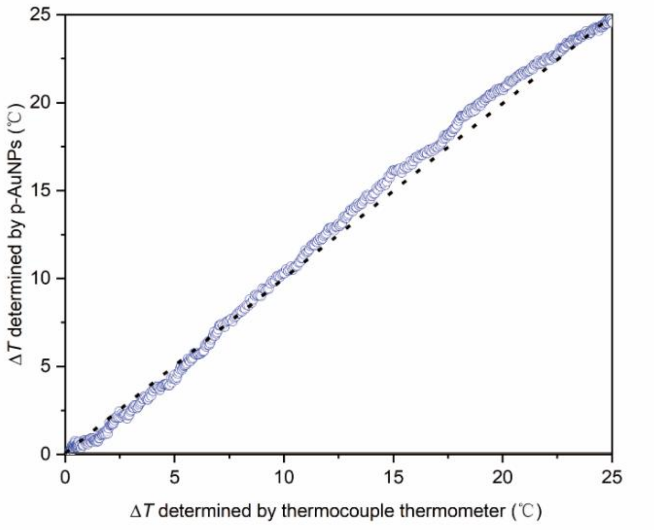

Fig. S4. The relationship between Δ*T* determined by thermocouple thermometer and Δ*T* determined by p-AuNPs in aqueous solution. The 1:1 line is shown as dotted line.

Fig. S5.

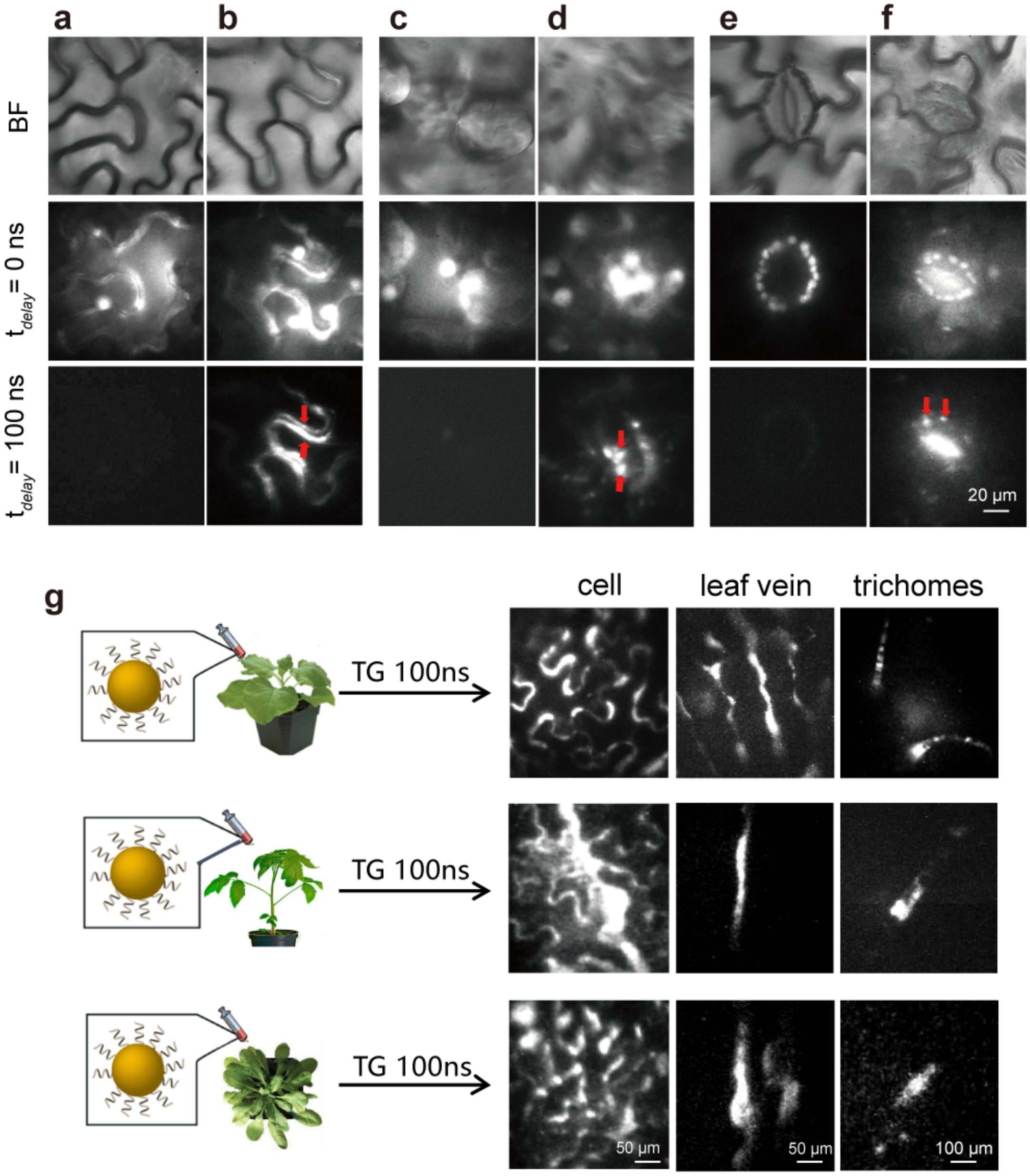

Fig. S5. The distribution of p-AuNPs in plants leaves.

a, **c**, **e**, The leaf without p-AuNPs. When the t_{delay} = 100 ns, there was no signal of the probes observed in the cell wall, cytoplasm, the stomata and the guard cell chloroplasts. **b**, **d**, **f**, The leaf was injected with the p-AuNPs. When the t_{delay} = 100 ns, the signal of the probes was observed in the cell wall, cytoplasm, the stomata and the guard cell chloroplasts, as indicated by the red arrows. **g**, The distribution of p-AuNPs fluorescence signals in three different plant leaves after a delay of 100 ns. After a delay of 100 ns, they were observed in cells, leaf veins, and trichomes of different plant leaves. For all experiment groups, about 20 μL p-AuNPs (80 $\mu g \cdot mL^{-1}$) was used for each leave.

Fig. S6.

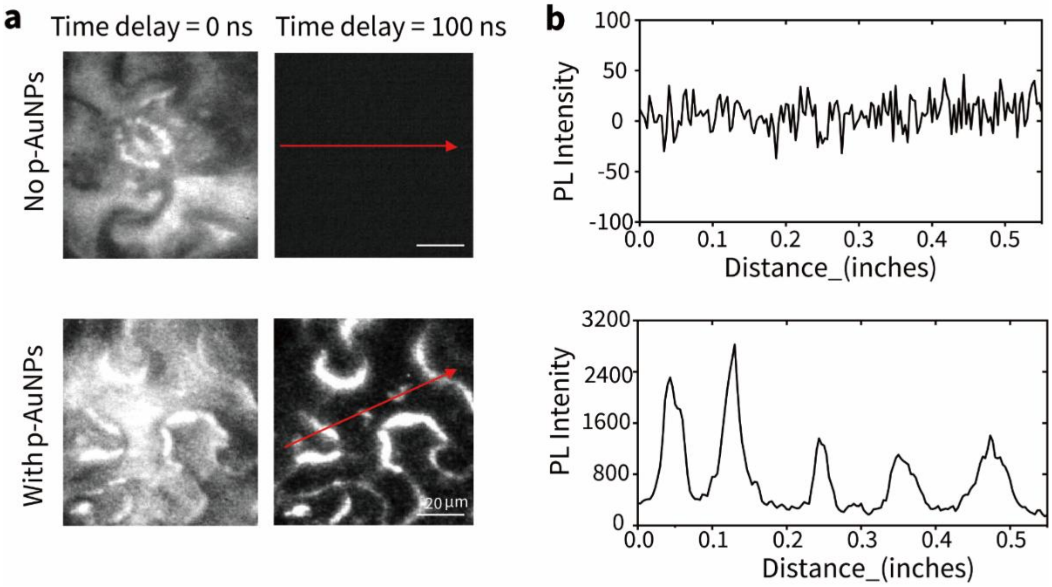

Fig. S6. The signal of p-AuNPs in the *N.benthamiana* leaves.
a, Comparison of the intensity between plant leaves with and without probes at a delay of 0 ns and 100 ns. **b**, The signal distribution with a delay of 100 ns at the red arrow in **a**. Scale bar: 20 μm.

Fig. S7.

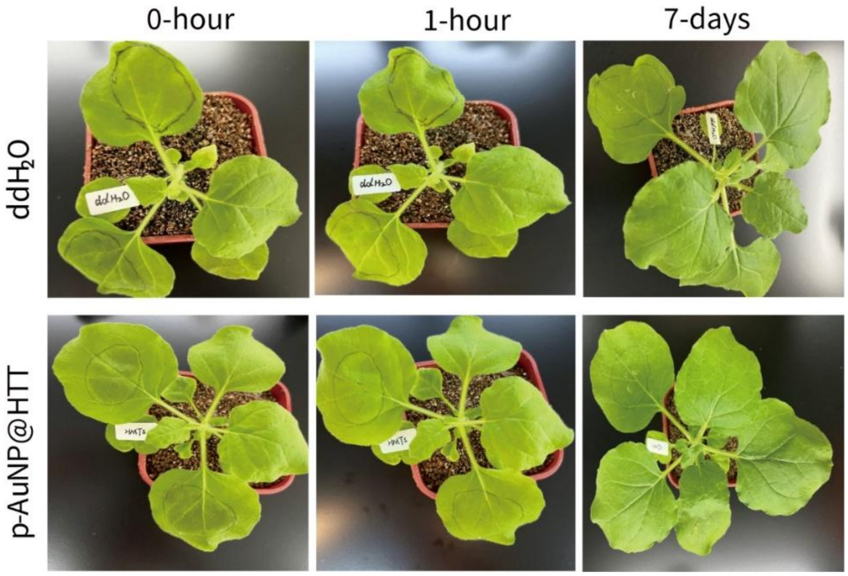

Fig. S7. Photos of *N.benthamiana* leaves prior to and post-infiltration with p-AuNPs.
Photos of *N.benthamiana* leaves were taken 0 hour, 1 hour and 7 days after infiltration with ddH_2O and p-AuNPs (50 μL, 80 μM). The circles have been used to delineate the wetted area.

Fig. S8.

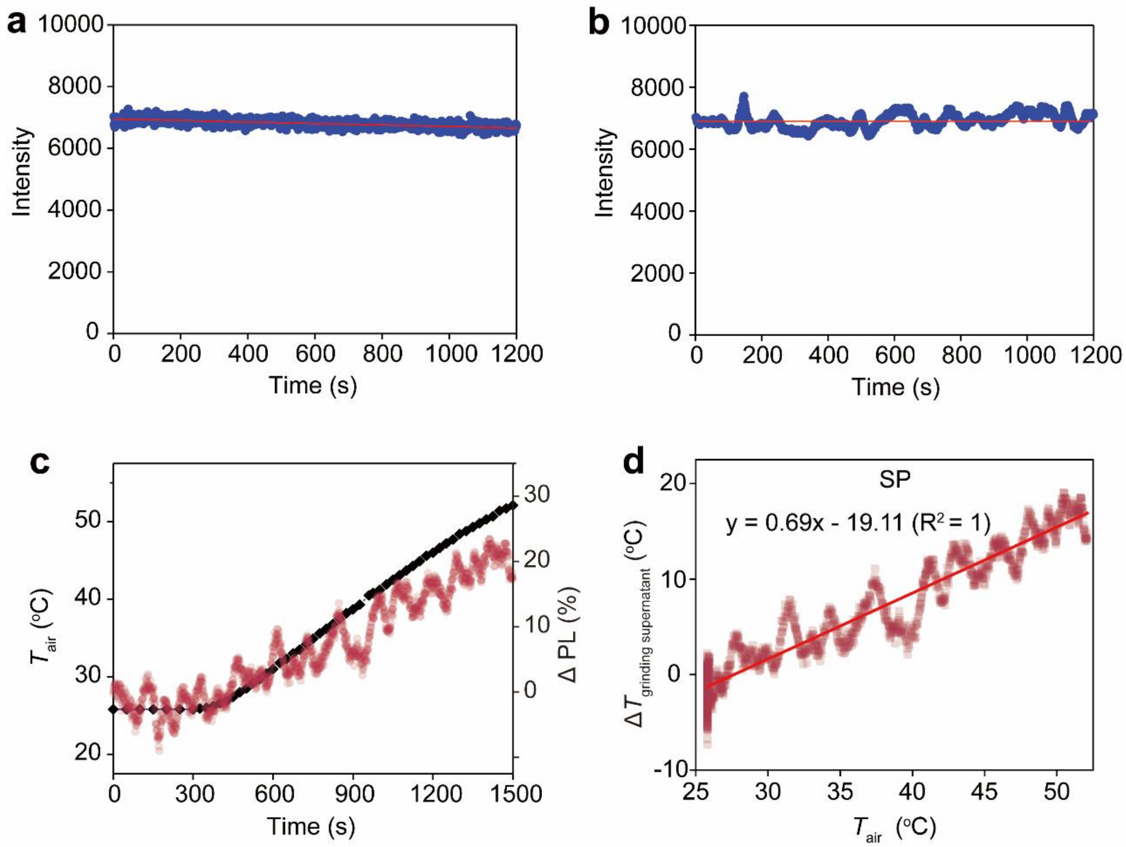

Fig. S8. The p-AuNPs in the leaf grinding liquid supernatant of *N.benthamiana*.
a, The intensity of the p-AuNPs (80 μM) in ddH_2O (50 μL, 80 μM). **b**, The intensity of the p-AuNPs (80 μM) in the supernatant of leaf grindings. **c**, The intensity of p-AuNPs and air temperature in supernatant of leaf grinding fluid with under heat stress. The black line indicates the air temperature measured by a thermocouple sensor, and the red curve indicates the photoluminescence from the probes. The initial PL intensity was defined as 0. **d**, The intensity of p-AuNPs changed with air temperature in supernatant of leaf grinding fluid. The initial PL intensity was defined as 0.

Fig. S9.

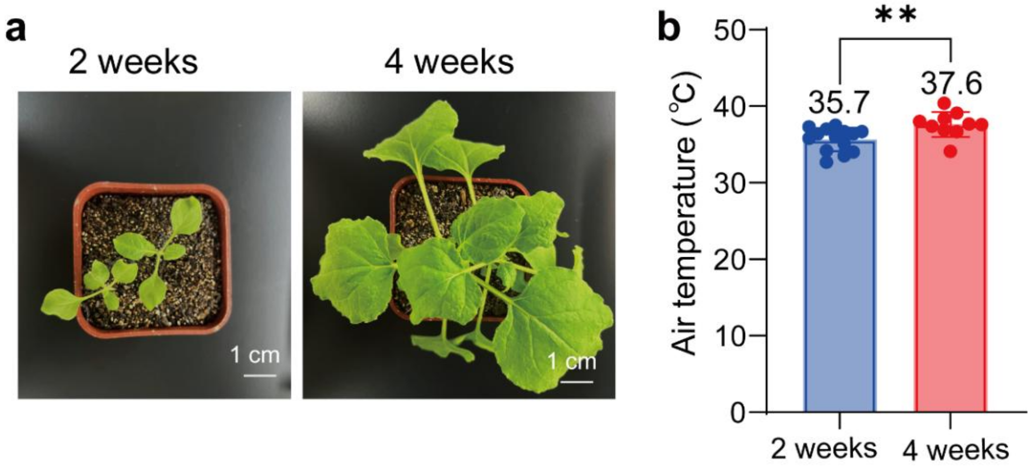

Fig. S9. The response of *N.benthamiana* leaves to environmental temperature at different stages.

a, *N.benthamiana* leaves at different stages, 2-week and 4-week leaves. **b**, Comparison of T_{TH} between 2-week and 4-week leaves. It was 35.7°C under 2-week and 37.6°C under 4-week. Two-tailed Student's *t*-test for comparison. $n = 10$. $^{**}p < 0.01$; n.s.: no Significant difference.

Fig. S10.

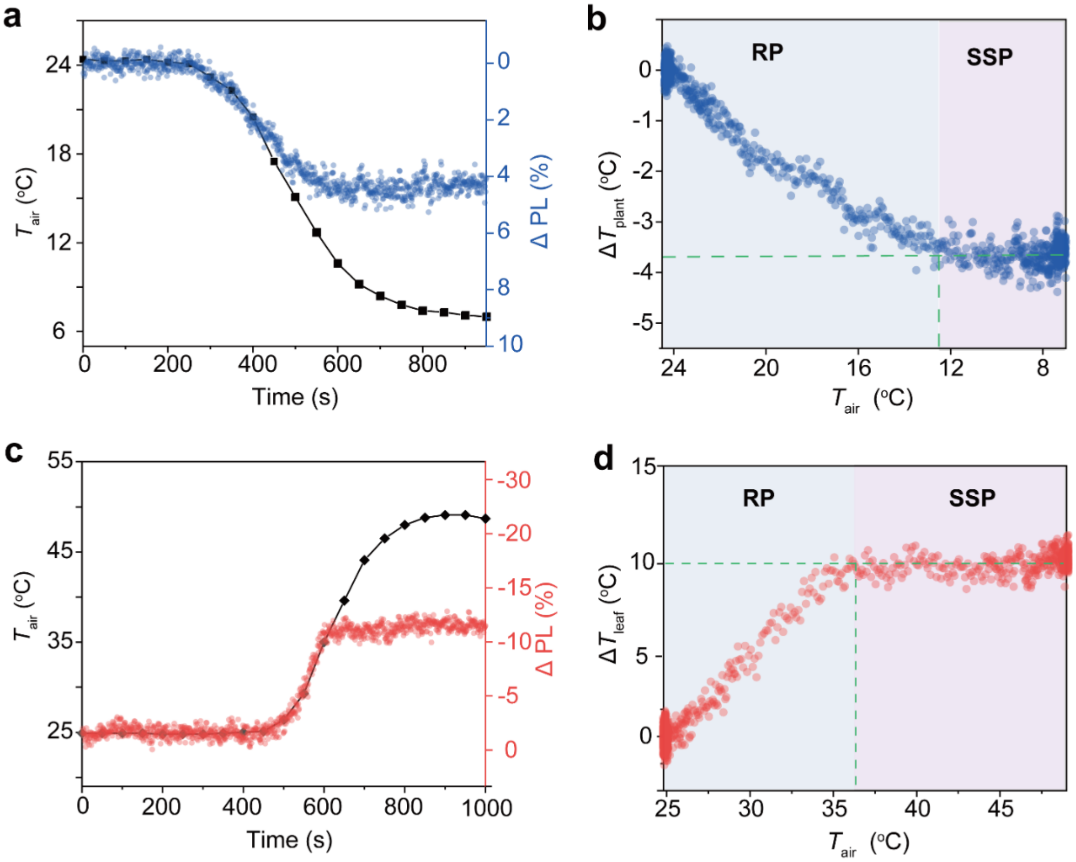

Fig. S10. The typical response of tomato leaves to temperature stress.
a, The typical PL intensity of p-AuNPs and air temperature in the tomato leaves as a function of time during cold stress. **b**, The leaf temperature changed along with air temperature during cold stress. Two phases, the response phase (RP) and the steady-state phase (SSP) could be observed. **c**, The PL intensity of p-AuNPs and air temperature in the tomato leaves as a function of time during heat stress. **d**, The leaf temperature change with air temperature during heat stress. Two phases, the response phase (RP) and the steady-state phase (SSP) could be observed. The initial PL intensity was defined as 0, and the black dots indicate the air temperature measured by a thermocouple sensor, and the blue and red circles indicates the photoluminescence from the probes.

Fig. S11.

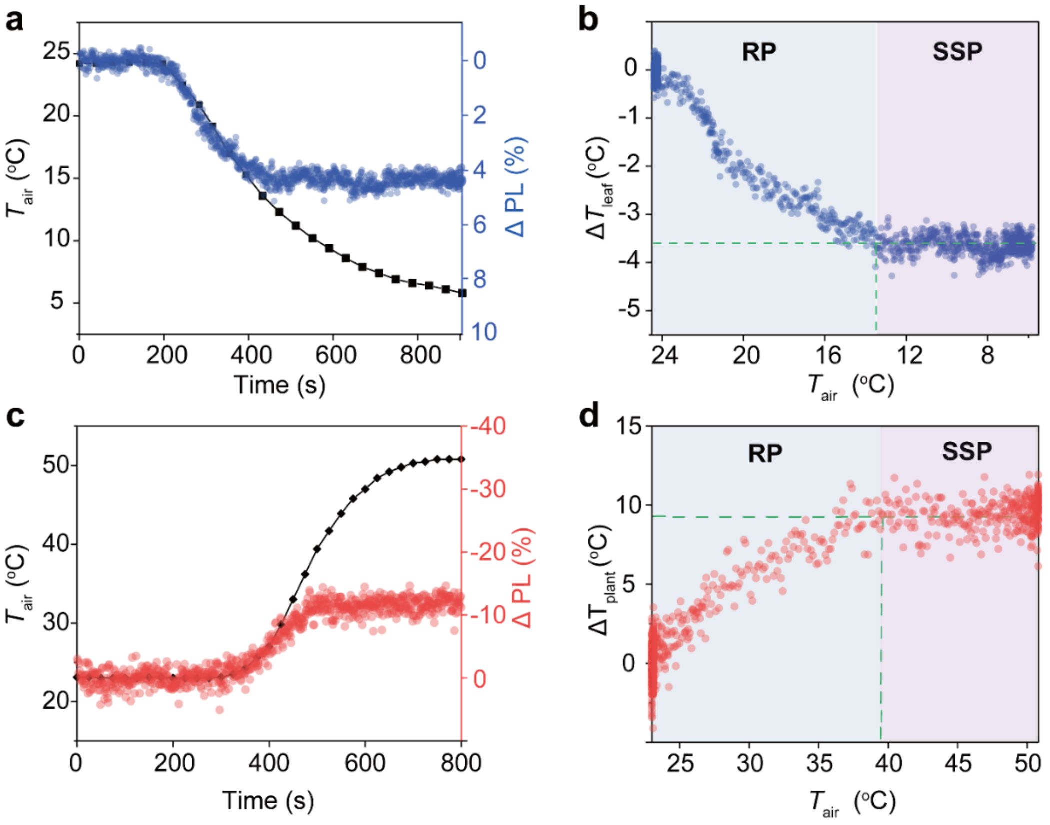

Fig. S11. The typical response of *Arabidopsis thaliana* leaves to temperature stress. **a**, The typical PL intensity of p-AuNPs and air temperature in the *Arabidopsis* leaves as a function of time during cold stress. **b**, The leaf temperature changed with air temperature during cold stress. Two phases, the response phase (RP) and the steady-state phase (SSP) could be observed. **c**, The PL intensity of p-AuNPs and air temperature in the *Arabidopsis* leaves as a function of time during heat stress. **d**, The leaf temperature changed with air temperature during heat stress. Two phases, the response phase (RP) and the steady-state phase (SSP) could be observed. The initial PL intensity was defined as 0, and the black dots indicate the air temperature measured by a thermocouple sensor, and the blue and red circles indicates the photoluminescence from the probes.

S12

Thermodynamic Modeling and Dynamic Parameter Fitting

To elucidate the microscale thermodynamic dynamics and targeted water-cooling mechanisms within plant cells, we developed a five-node lumped-parameter thermodynamic model. Biologically, the cell wall and intercellular spaces constitute the continuous apoplast network. When subjected to environmental heat stress, the highly hydrated apoplast in the substomatal cavity serves as the primary interface for intense heat exchange and water phase change. Given the structural identity of the porous cell wall matrix and the rapid local thermodynamic equilibrium (LTE) at the microscale, the experimentally measured cell wall temperature (T_{cw}) is physically equivalent to the apoplastic temperature (T_{apo}) in our model ($T_{cw} \approx T_{apo}$). The evaporation of water from the apoplast acts as a microscale cooling engine. Its evaporative heat loss power (latent heat of transpiration, Q_t) is defined as:

$$Q_t = Q_{apo0} \cdot \exp[k_{trans} \cdot (T_{apo} - T_{a0})]$$

where Q_{apo0} is the fixed baseline evaporative power at the reference ambient temperature (T_{a0}) and k_{trans} is the fitted evaporative response index[1].

Under environmental heat stress, plant cells activate a targeted intracellular advection cooling network mediated by water channels (AQPs) on the plasma and organelle membranes[2]. Rather than using empirical linear correlations, the advective heat transfer (thermal convection, Q_i) across specific membranes is mathematically reconstructed based on rigorous thermodynamic first principles. The magnitude of this convective heat transfer is fundamentally determined by the transmembrane mass flux of water. Physically, this water flux is governed by two key factors: the osmotic pressure gradient driving the flow, and the hydrodynamic conductance of the membrane channels[3]. Crucially, both factors exhibit strong temperature dependency and can be mathematically expressed as functions of the temperature variation. The osmotic driving force is modeled according to the van 't Hoff law, where the active intracellular accumulation of osmolytes dynamically scales with the local temperature rise. Concurrently, the membrane channel conductance—dictating the AQP gating efficiency and lipid bilayer fluidity—follows a strict temperature-dependent exponential relationship governed by Arrhenius kinetics[4-6].By integrating these temperature-dependent functions, the advective heat transfer Q_i is formulated as:

$$Q_i = \lambda_i \cdot [(T_{a0} + \Delta T_{apo}) \cdot (1 + \beta \Delta T_{apo})] \cdot \exp[\frac{E_a}{R}(\frac{1}{T_{a0}} - \frac{1}{T_{a0} + \Delta T_{apo}})] \cdot \Delta T_{local}$$

where λ_i represents the basal hydrodynamic conductance for a specific intracellular pathway, β is the osmotic accumulation coefficient reflecting active physiological adjustment, E_a is the activation energy for AQP gating and membrane phase transition, R is the ideal gas constant, and ΔT_{local} denotes the local temperature difference between the interacting compartments driving the advective heat transfer.

Governed by the First Law of Thermodynamics (energy conservation), the transient heat transfer and temperature evolution within the cellular network are strictly dictated by a system of coupled ordinary differential equations (ODEs). This ODE system abstracts the microscale cellular compartments into lumped thermodynamic nodes, comprehensively reconstructing the energy balance dynamics under heat stress by precisely quantifying four core thermodynamic fluxes: interfacial thermal conduction, transmembrane thermal convection (Q_i), apoplastic latent heat of transpiration (Q_t), and localized basal metabolic heat generation (G_i). The governing equations are explicitly expanded as follows:

Stomatal layer:

$$C_s \frac{dT_s}{dt} = hA_{air}(T_{air} - T_s) - hA_{s-apo}(T_s - T_{apo}) \qquad (1)$$

Apoplast:

$$C_{apo}\frac{dT_{apo}}{dt} = hA_{s-apo}(T_s - T_{apo}) - hA_{apo-cyt}(T_{apo} - T_{cyt}) - Q_t + Q_{apo-c} \quad (2)$$

Cytosolic:

$$C_{cyt}\frac{dT_{cyt}}{dt} = hA_{apo-cyt}(T_{apo} - T_{cyt}) - Q_{apo-c} - hA_{cyt-chl}(T_{cyt} - T_{chl}) + Q_{chl} - hA_{cyt-other}(T_{cyt} - T_{other}) + Q_{other} + G_{cyt} \quad (3)$$

Chloroplasts:

$$C_{chl}\frac{dT_{chl}}{dt} = hA_{cyt-chl}(T_{cyt} - T_{chl}) - Q_{chl} + G_{chl} \quad (4)$$

Non-photosynthetic organelles:

$$C_{other}\frac{dT_{other}}{dt} = hA_{cyt-other}(T_{cyt} - T_{other}) - Q_{other} + G_{other} \quad (5)$$

Here, hA denotes the respective boundary conductive heat transfer coefficients, and T_{air} is the dynamic ambient temperature. The convective terms (Q_{apo-c} , Q_{chl} , Q_{other}) dynamically substitute the general Q_i formula to trace the directional advective cooling driven by the transpiration stream from inner compartments towards the apoplast.

Before simulating the dynamic response to heat stress, it is imperative to establish the baseline thermodynamic equilibrium of the cellular system. At the initial time ($t = 0$), the system is assumed to be in a perfect steady state under the reference ambient temperature ($T_{a0} = 24.0$°C). Under this steady-state assumption, the time derivatives of temperature for all nodes are zero. By applying this condition to the ODE system (Equations 1-5), we can analytically derive the unmeasurable basal metabolic heat generation (G_i) for each cellular compartment. For example, the initial heat generation in the cytoplasm (G_{cyt}) is calculated as the net thermal energy required to balance the conductive and convective heat exchanges with the apoplast and the internal organelles at $t = 0$.

Furthermore, to prevent the high-dimensional optimization space from converging to biologically impossible local minima, structural heat capacities (C_i) and baseline overall heat transfer coefficients (hA_{i-j}) were strictly fixed a priori based on cellular morphometric constraints (Table S1). Given the highly hydrated nature of plant cells, the specific heat capacity of water was uniformly applied to all cellular compartments. The structural heat capacity for each node (C_i) was then derived by scaling this uniform water heat capacity by its respective morphometric volume fraction.

Parameter estimation was performed using the interior-point method for constrained nonlinear optimization, globally aligning the simulated spatial temperature profiles with the experimental data. Through the global unconstrained inversion driven purely by the experimental dynamics, the optimization algorithm precisely quantified the free parameters based on thermodynamic first principles (Table S2). This includes the initial absolute temperatures prior to heat stress (T_{i0}), the evaporative response index (k_{trans}), the osmotic accumulation coefficient (β), the macroscopic activation energy for AQP gating and membrane phase transition (E_a), and the basal hydrodynamic conductances (λ_i) governing the targeted transmembrane water fluxes.

Table S1. Fixed thermodynamic constants used in the model.

Symbol	Value (a.u.)	Biological Representation
C_s	1.0×10^{-5}	Surface/Stomatal layer thermal mass
C_{apo}	2.0×10^{-5}	Highly hydrated apoplast network
C_{cyt}	5.0×10^{-5}	Cytosolic thermal pool
C_{chl}	1.0×10^{-5}	Core chloroplasts

C_{other}	1.0×10^{-4}	Non-photosynthetic organelle
hA_{air}	2.0×10^{-3}	Ambient air to surface boundary conduction
hA_{s-apo}	5.0×10^{-3}	Surface to apoplast conduction
$hA_{apo-cyt}$	5.0×10^{-5}	Trans-plasma membrane conduction
$hA_{cyt-chl}$	5.0×10^{-4}	Cytosol to chloroplast conduction
$hA_{cyt-other}$	5.0×10^{-4}	Cytosol to non-photosynthetic organelles
Q_{apo0}	4.0×10^{-4}	Evaporative power at baseline ambient temperature

Table S2. Optimized parameters via dynamic parameter inversion.

Symbol	Optimized Value	Description
T_{apo0}	24.21°C	Baseline apoplast temperature
T_{cyt0}	26.73°C	Baseline cytosolic temperature
T_{other0}	26.52°C	Baseline non-photosynthetic organelles temp
T_{chl0}	35.92°C	Baseline chloroplast temp
k_{trans}	0.4083	Exponential response index to thermal stress
β	0.1503 /K	Osmotic solute accumulation coefficient
E_a	82.00 kJ/mol	Activation energy for AQP gating/phase transition
λ_{apo-c}	0.1741	Background cytosol-to-apoplast fluidic coupling
λ_{other}	0.3099	Water flux coupling to massive vacuole
λ_{chl}	0.6316	Targeted water flux coupling to chloroplasts

References

1 Gates, D. M. Transpiration and Leaf Temperature. *Annual Review of Plant Physiology* **19**, 211-238, doi:10.1146/annurev.pp.19.060168.001235 (1968).

2 Kapilan, R., Vaziri, M. & Zwiazek, J. J. Regulation of aquaporins in plants under stress. *Biol Res* **51**, 4, doi:10.1186/s40659-018-0152-0 (2018).

3 Steudle, E. The cohesion-tension mechanism and the acquisition of water by plant roots. *Annual review of plant physiology and plant molecular biology* **52**, 847-875, doi:10.1146/annurev.arplant.52.1.847 (2001).

4 Wahid, A., Gelani, S., Ashraf, M. & Foolad, M. R. Heat tolerance in plants: An overview. *Environmental and Experimental Botany* **61**, 199-223, doi:10.1016/j.envexpbot.2007.05.011 (2007).

5 Ionenko, I. F., Anisimov, A. V. & Dautova, N. R. Effect of temperature on water transport through aquaporins. *Biologia Plantarum* **54**, 488-494, doi:10.1007/s10535-010-0086-z (2010).

6 Maurel, C. *et al.* Aquaporins in Plants. *Physiol Rev* **95**, 1321-1358, doi:10.1152/physrev.00008.2015 (2015).